iScience

CellPress
OPEN ACCESS

Article

Optically induced quantum transitions in direct probed mesoscopic $NbSe_2$ for prototypical bolometers

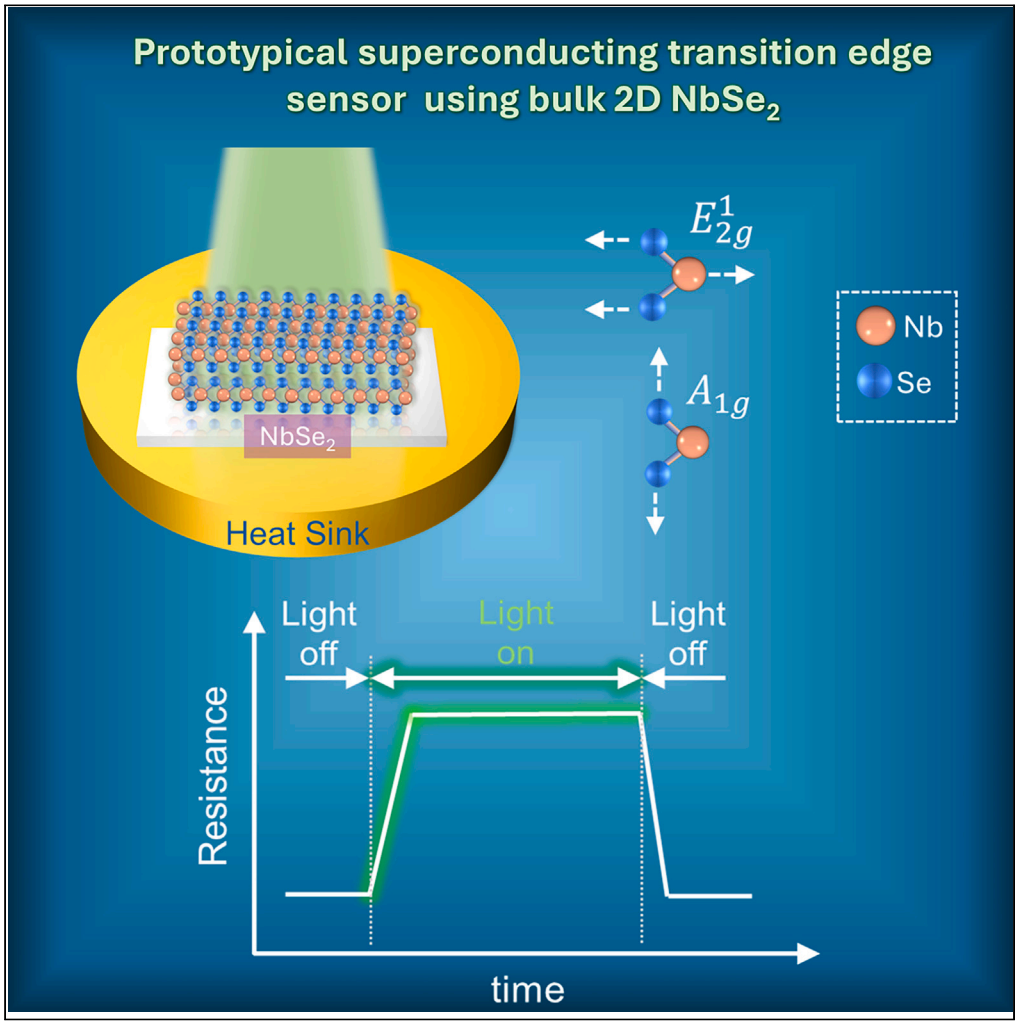

Kishan Jayanand, Gustavo A. Saenz, Sergiy Krylyuk, ..., Zhonghe Liu, Weidong Zhou, Anupama B. Kaul

anupama.kaul@unt.edu

Highlights

Incoming optical radiation absorbed by superconducting $NbSe_2$

Heat generated from absorption causes switching to normal state

Switching characteristics depend on wavelength of incoming radiation

Superconducting $NbSe_2$ shows promise for bolometers and radiation detectors

Jayanand et al., iScience 27, 110818
September 20, 2024
https://doi.org/10.1016/j.isci.2024.110818

iScience

CellPress
OPEN ACCESS

Article

Optically induced quantum transitions in direct probed mesoscopic $NbSe_2$ for prototypical bolometers

Kishan Jayanand,[1] Gustavo A. Saenz,[2] Sergiy Krylyuk,[3] Albert V. Davydov,[3] Goran Karapetrov,[4] Zhonghe Liu,[5] Weidong Zhou,[5] and Anupama B. Kaul[1,2,6,*]

SUMMARY

Superconducting transition-edge sensors (TES) have emerged as fascinating devices to detect broadband electromagnetic radiation with low thermal noise. The advent of metallic transition metal dichalcogenides, such as $NbSe_2$, has also created an impetus to understand their low-temperature properties, including superconductivity. Interestingly, $NbSe_2$-based sensor within the TES framework remains unexplored. In this work, direct-probed superconducting $NbSe_2$ absorbers led to a proof-of-concept demonstration for the transduction of incoming light to heat, where a thermodynamic superconducting phase transition in $NbSe_2$ was evident to switch it to the normal state, when biased below its superconducting transition temperature. A wavelength-dependent response of its optical absorption properties was observed, based on the incident optical excitation source used. Furthermore, extensive optical characterization studies were conducted using Raman spectroscopy, where the in-plane and out-of-plane thermal conductivity was empirically determined. Our results open possibilities for the use of $NbSe_2$ in superconducting radiation detectors, including in a TES framework.

INTRODUCTION

Layered two-dimensional (2D) materials have intrigued the research community since the mechanical exfoliation of graphene in 2004,[1] where their outstanding optical, mechanical, and electronic properties have been at the heart of fundamental studies, including in transition metal dichalcogenides (TMDs).[2,3] Studies on TMDs have opened up opportunities for exploring their use in photodetectors,[4] zero-dimensional (0D) cage molecule-2D hybrids,[5] and quantum multibody systems.[6] The TMDs are present in five polytypes: tetragonal (1T), hexagonal (2H), rhombohedral (3R), orthorhombic (1T′), and monoclinic (Td). Each layer consists of a transition metal *M* (e.g., Mo, Nb, W, and Re) sandwiched between two chalcogen *X* (e.g., S, Se, and Te) atomic planes that form the *X-M-X* tri-planar architecture, with the MX_2 stoichiometry. In this crystalline structure, strong in-plane covalent bonding arises between the *X-M-X* complex, while the out-of-plane bonding between adjacent *X-X* interactions is weak, arising from van der Waals coupling.[7] The electronic structure of TMDs ranges from the typical *d*-block group VI semiconducting (e.g., MoS_2, $MoSe_2$, WS_2, and WSe_2) to the metallic or semi-metallic (e.g., TaS_2, $TaSe_2$, NbS_2, $NbSe_2$) group V binary chalcogen compounds.[8] In the case of group VI semiconducting TMDs, their out-of-plane quantum confinement leads to bandgap tunability, and the transition from indirect bandgap to direct bandgap optical transitions being a characteristic feature.[1,9]

While the semiconducting TMDs have garnered significant attention from the broader research community, the body of work on superconducting 2D materials, particularly $NbSe_2$, also a TMD, appears to be less extensive. In particular, $NbSe_2$ has distinctive electronic and magnetic properties including emergent superconductivity, which coexists with incommensurate charge density wave (ICDW) states. The latter phenomenon is attributed to a periodic modulation of conduction electrons accompanied with lattice distortions at temperatures *T* below 33.5 K.[10] In single unit cell thick layers of $NbSe_2$ superconductivity is realized via Ising spin pairing due to broken inversion symmetry.[11]

Cryogenically induced superconducting transitions are at the heart of superconducting tunnel junctions relying on the Josephson effect[12] in the superconductor-insulator-superconductor (SIS) configuration, as well as superconducting-quantum-interference-devices (SQUIDs) for high-speed superconductor electronics.[13,14] The Josephson junction is comprised of an ultra-thin insulator film sandwiched between two superconducting layers which forms the basis for quantum-limited detection, pivotal in astrophysics applications,[15] along with superconducting qubits for quantum computing.[16] The latter is a rapidly growing area in recent times toward national security needs involving the broader

[1]Department of Materials Science and Engineering, University of North Texas, Denton, TX 76207, USA
[2]Department of Electrical Engineering, University of North Texas, Denton, TX 76207, USA
[3]Material Science and Engineering Division, National Institute of Standards and Technology, Gaithersburg, MD 20899, USA
[4]Department of Physics, Drexel University, Philadelphia, PA 19104, USA
[5]Department of Electrical Engineering, University of Texas at Arlington, Arlington, TX 76019, USA
[6]Lead contact
*Correspondence: anupama.kaul@unt.edu
https://doi.org/10.1016/j.isci.2024.110818

quantum information science community. More recently lower-dimensional materials such as 0D nanoparticles, 1D nanowires, and 2D materials have been explored for their use in single photon detection, a key component of quantum information science employing photons.[17]

Another device that leans on superconducting properties for its operation is the transition edge sensor (TES). Here, incoming photons from incident electromagnetic radiation interact with the superconducting sensor which is biased on the steeply rising edge in the resistance R versus T characteristic of the TES. Incoming radiation causes local heating to propel the superconducting sensor to its normal state, forming the basis for radiation detection where sensitivity toward the quantum-limit is a fundamental goal.[18] The TES has been implemented for non-destructive analysis of nuclear materials,[19] neutrino detection,[20] optical and microwave frequency detection[21,22] on the European Athena satellite,[23] and South Pole Telescope,[24] as well as electron-beam ion traps (EBIT).[25] The hot-electron bolometer (HEB), based on direct detection or mixing, outperforms SIS and Schottky diodes in astronomical observations significantly above 1 THz which were used on the Herschel space observatory.[26] The microwave kinetic inductance detector (MKID),[27] the superconducting nanowire single-photon detector (SNSPD),[28] and the superconducting stripline detector (SSLD)[29] are other variants of detectors relying on superconducting materials. In many situations, the aforementioned devices exhibit low-thermal noise and high sensitivity.[18,30-31] Superconducting films employed in the aforementioned detectors typically rely on materials such as Mo,[32] Nb,[33] NbN,[34] and high-T_c superconductors such as YBCO[35] and MgB_2.[36]

Although elemental or compound superconducting materials have been extensively studied for their use in TES devices, including some material systems such as Nb and YBCO where investigations have spanned several decades, 2D materials on the other hand, are far less explored for TES applications. Elemental superconductors such as Mo shows a superconducting transition temperature $T_c \sim 0.9$ K, while Nb exhibits $T_c \sim 9$ K. Binary 3D crystalline compounds, such as the nitride of refractory Nb, i.e., NbN yields T_c in the range of ~12–16 K dependent on its crystalline quality and offers a more direct comparison to the selenide of Nb which takes up a 2D crystalline host lattice in the form of $NbSe_2$. In comparison to the aforementioned 3D crystalline materials, either elemental or binary, 2D $NbSe_2$ exhibits layer-dependent properties, a feature not commonly observed in 3D crystalline material systems, stemming from the out-of-plane van der Waals bonding in the latter. For example, previous studies conducted on $NbSe_2$ have demonstrated a thickness-dependent magnetic susceptibility and superconducting response.[37] This layer-dependent response also likely poses intriguing possibilities when $NbSe_2$ is used as the absorber material in TES architecture, providing another exciting degree of freedom to tune its interaction to incoming radiation. The current study considered in this work on bulk $NbSe_2$ should thus serve as an important benchmark and stepping-stone to extended such empirical analysis in the future for the validation of theoretically proposed phenomena for TES devices based on $NbSe_2$ in the limit of monolayers and thickness-dependent device parameters. Additionally, Xi et al.[38] previously demonstrated layer-dependent gate tunability of the superconducting transition of $NbSe_2$, where the transition temperature and superconducting bandgap maybe tuned externally. Through layer engineering and electrostatic tuning, $NbSe_2$ may serve as a candidate bolometer material for high-energy particle detection, as well as a single photon detector for quantum information science applications. Furthermore, large area detectors, such as long-range telescopes, may benefit from the arrangement of $NbSe_2$ pixel arrays capable of capturing and detecting a wide spectral range of energies, on-demand, via layer engineering and electrostatic tuning of the crystallites.

The 2D TMD materials family has grown at a rapid pace over the last decade, and much attention has been placed on the large-area synthesis and manufacturing of these van der Waals solids.[39] Approaches for the large-scale synthesis of 2D materials include chemical vapor deposition (CVD), liquid exfoliation, and wet chemical synthesis, to mention a few. Of the aforementioned growth approaches, CVD offers the most potential for generating high-crystalline quality materials, while at the same time being largely compatible with the infrastructure of today's microelectronics industry and semiconductor process technology.[40] Recent work has demonstrated the ability to produce high-quality $NbSe_2$ with thicknesses control using CVD processes.[41–43] This highlights the possibility of manufacturing high-grade and crystalline quality $NbSe_2$ toward future scalable platforms and for the deployment of superconducting $NbSe_2$ toward important applications, including TES devices.

Furthermore, $NbSe_2$ is a refractory material with a melting point >1,573 K from which a high bond strength, as well as high mechanical stability, maybe inferred.[44] Specifically, the bulk modulus of $NbSe_2$ is reported to be ~52 GPa,[45] which is similar in magnitude, to first order, to Silicon's bulk modulus (~130 GPa),[46] where the latter is widely recognized as a robust mechanical support structure for micro-electro-mechanical systems (MEMS), as well as TES devices. Thus, we expect $NbSe_2$ to offer similar structural stability attributes, while its chemical and air-stability is a topic discussed in more detail in the section "Synthesis and materials characterization of 2H-$NbSe_2$", where experimental analysis was facilitated by Raman spectroscopy and energy dispersive X-ray spectroscopy (EDS). Such spectroscopy analysis revealed no observable degradation for our samples when they were exposed to radiation under ambient conditions, corroborating its stabile nature, which should be beneficial for practical TES devices.

In this work, we demonstrate the use of a bulk $NbSe_2$, as a superconducting bolometer when it couples to incoming electromagnetic radiation. Here, a change in temperature is sensed as a result of absorption of the electromagnetic radiation focused on the crystal, causing the optical-to-thermal transduction to arise from the superconducting-to-normal transition. Direct probing of the bulk $NbSe_2$ crystal in a cryogenic probe stage with optically pumped incoming radiation spanning the ultraviolet (UV, λ = 405 nm), visible (VIS, λ = 660 nm), and near-infrared (NIR, λ = 1060 nm) via an optical fiber at cryogenic temperatures allowed us to observe the superconducting-to-normal state transition. Time-resolved measurements were also conducted with these lasers, which enabled us to estimate switching parameters of bulk $NbSe_2$-based prototypical TES device. The in-plane and out-of-plane first-order temperature and laser power dependent coefficients of the bulk $NbSe_2$ crystallite were tabulated by analyzing the Raman peak shifts with respect to temperature T and power P, which provided insights into the in-plane and out-of-plane thermal conductivities, where the former was found to be a factor of two higher. Our prototypical demonstration shows the optical-to-thermal transduction in the superconducting transition of bulk 2H-$NbSe_2$, driven solely by incoming

optical radiation. This work is well positioned to open opportunities for the use of $NbSe_2$ and other superconducting dichalcogenides in superconducting bolometers in the future.

RESULTS

Synthesis and materials characterization of 2H-$NbSe_2$

The 2H-$NbSe_2$ crystals were grown using the chemical vapor transport (CVT) method with $SeBr_4$ as the transport agent, and the details of the growth is discussed in the STAR Methods. Powder X-ray diffraction (XRD) scans depicted in Figure 1A confirms the hexagonal crystal structure of the obtained 2H-$NbSe_2$ flakes (space group P63/mmc). Materials Data Inc (MDI) Jade 6.5 software (Livermore, CA 2015) was used to calculate the lattice parameters of our 2H-$NbSe_2$ crystallites where the parameters were determined to be $a_1 = a_2 \sim 3.445$ Å and $a_3 \sim 12.548$ Å, which are comparable to lattice constants previously reported[47] for 2H-$NbSe_2$ ($a_1 = a_2 = 3.449$ Å and $a_3 = 12.54$ Å). Post growth, the CVT grown $NbSe_2$ crystallites were stored in a vacuum desiccator to minimize air-exposure and possiblity of consequent degradation.[48]

The bulk $NbSe_2$ flakes were further examined using Raman spectroscopy. The lattice of 2H-$NbSe_2$ is reported to encompass A_u, B_g, B_u, A_g, E_u, and E_g, vibrational modes of which one out-of-plane phonon mode (A_{1g}), and three in-plane phonon modes (E_{1g}, E^1_{2g} and E^2_{2g}) are reported to be Raman active.[49] A schematic of the Raman active vibrational modes in $NbSe_2$ is shown in Figure 1B. In contrast, Raman inactive modes correspond to asymmetric vibrational modes, either stretched or bent, which are detected using Fourier transform infrared spectroscopy (FTIR). In our sample, a thick $NbSe_2$ crystal was placed on a 270 nm thick thermal SiO_2 layer on a Si substrate for high optical contrast (see schematic in Figure 1C). The approximate dimensions of the $NbSe_2$ crystallite used in the following investigations were measured to be 2 mm × 1 mm × 13 μm (length × width × height). From the Raman analysis, the vibrational modes occur at ≈ 228.2 cm^{-1} and ~238.7 cm^{-1} which are assigned to the A_{1g} and E^1_{2g} modes, respectively, as shown in Figure 1D, and the data are in close agreement with previous reports.[50] The broad line around 180 cm^{-1} is called the soft mode due to a second-order scattering mechanism,[51] and its analysis is beyond the scope of this paper. The E^2_{2g} vibrational mode is reported to occur at ~ 29.6 cm^{-1}, and we did not observe this mode due to limitations of our micro-Raman instrumentation. Furthermore, the E_{1g} mode signal intensity is reported to be very low because of the small Raman cross-section.[49]

The T-dependent Raman spectroscopy measurements were then conducted from $T \sim 80$ K where cooling was done using liquid nitrogen (LN2), and a heater was used to warm up the sample up to room $T \sim 298$ K. The laser was stabilized at a constant laser power $P \sim 0.84$ mW at which an appreciable signal-to-noise (S/N) ratio was obtained, without inducing damage to the bulk $NbSe_2$ crystallite. The E^1_{2g} and A_{1g} modes were analyzed using Gaussian peak-fitting to extract the Raman shift. The contour plot in Figure 2A illustrates the Raman map as a function of T for our $NbSe_2$ crystallite. From the data presented in Figure 2B, the in-plane E^1_{2g} and out-of-plane A_{1g} modes were red-shift linearly as T increased from 80 K to 298 K. The first-order T-dependent behavior for the E^1_{2g} and A_{1g} modes was analyzed using,[52]

$$\omega(T) = \omega_0 + \chi T \quad \text{(Equation 1)}$$

where $\omega(T)$ is the Raman peak position as a function of T, ω_0 is the vibrational frequency at 0 K, and $^{\chi}$ is the first-order T coefficient extracted from the linear fit. In Equation 1, the influence of the higher-order T coefficient term ($\chi^2 T^2$)[53] was not examined given that the higher order non-linear trends were not apparent in our data in Figure 2C. Furthermore, the influence of the non-linear $\chi^2 T^2$ term has been previously reported in some TMDs only at $T > 350$ K,[54] while our measurements were well below this T range. From Equation 1, we find that $\left|\chi_{E^1_{2g}}\right| \approx$ 0.0410 cm^{-1}/K and $\left|\chi_{A_{1g}}\right| \sim$ 0.0174 cm^{-1}/K, as shown by the top and bottom panels in Figure 2C.

Next, the Raman shift of the modes was analyzed as a function of the incident optical excitation power P of the laser, shown in Figure 2D at room T. An increase in P causes an ensuing increase in T locally, which likely results in thermal dilation within the crystal, inducing a shift in the vibrational phonon spectrum. The first-order power P coefficient is described as follows,

$$\omega(P) = \omega_{P0} + \left(\frac{\delta\omega}{\delta P}\right)P \quad \text{(Equation 2)}$$

where $\omega(P)$ is the Raman peak position as a function of laser excitation power P, ω_{P0} is the vibrational frequency at $p = 0$ W, $\delta\omega/\delta P$ is the first-order power P coefficient which denotes the change in the A_{1g} and E^1_{2g} peak positions with increasing laser power P. Incidentally, with Gaussian peak position fitting to the laser power P-dependent Raman spectra presented in the inset of Figure 2D, we observe a red-shift in the A_{1g} and E^1_{2g} peaks with increasing laser power P over the entire range from low P (~11.7 μW) to high P (~4700 μW), though two regimes were evident where $\delta\omega/\delta P$ changed more rapidly up to 840 μW, as shown in Figure 2D. Additionally, the laser power P-dependent trend observed in $\delta\omega/\delta P$ (see Figure 2D) was found to be reversible upon reduction of laser power P from 4,700 μW to 11.7 μW. We believe the slower change in $\delta\omega/\delta P$ above P = 840 μW may be due to the influence of the higher-order non-linear term ($[(\delta^2\omega/\delta P^2)P^2]$) which was not considered in Equation 2 for our computation. In the low P range of 11.7 μW–840 μW, our data analysis led us to determine $|\delta\omega/\delta P|_{(A_{1g})} \sim$ 2.9 cm^{-1}/mW and $|\delta\omega/\delta P|_{(E^1_{2g})} \sim$ 3.9 cm^{-1}/mW using Equation 2. As a result, the thermal conductivity k is extracted using the following,[55]

$$k = \chi\left(\frac{1}{2\pi z}\right)\left(\frac{\delta\omega}{\delta P}\right)^{-1} \quad \text{(Equation 3)}$$

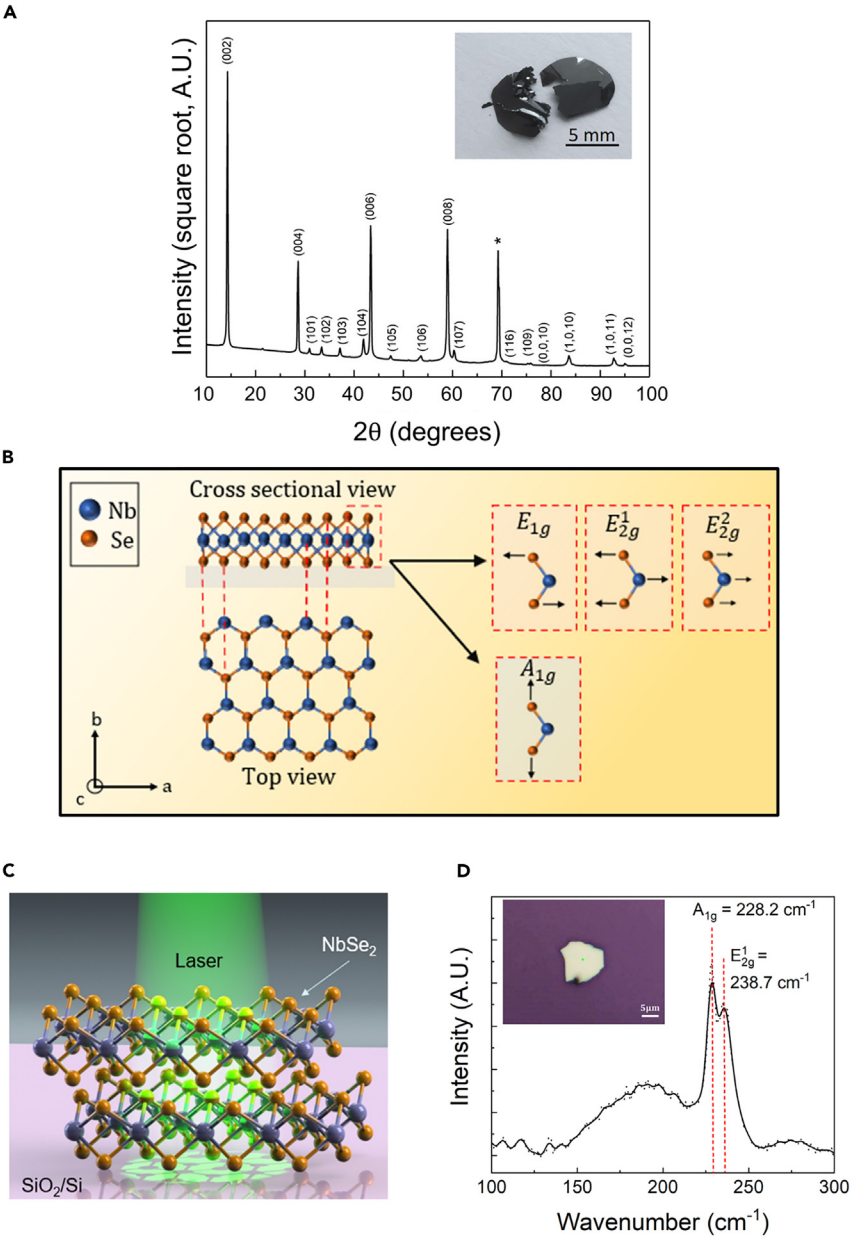

Figure 1. $NbSe_2$ crystal structure and phonon modes

(A) Powder XRD diffraction scans of *as grown* 2H-$NbSe_2$. The peak at 69.3° denoted with * refers to the Si (400) reflection from the sample holder. Inset shows a representative picture of CVT grown $NbSe_2$ flakes.

(B–D) Raman spectroscopy of 2H-$NbSe_2$, where the crystal structure of 2H-$NbSe_2$ (top and cross-sectional views) are shown in (b)-left, while the Raman active vibrational modes comprising of the out-of-plane A_{1g} and the in-plane E_{1g}, E^1_{2g}, E^2_{2g} modes are shown in (b)-right.

(C) Schematic of the 2H-$NbSe_2$ crystal placed on an SiO_2/Si substrate used for the micro-Raman measurements excited with a 532 nm laser source.

(D) Raman spectra gathered at room *T* for pristine 2H-$NbSe_2$ shown in the optical micrograph of the inset, where the vibrational modes are located at ~ 228.2 cm^{-1} and 238.7 cm^{-1}, corresponding to the A_{1g} and E^1_{2g} Raman modes, respectively.

where $^{\chi}$ is as described previously, and *z* is the thickness of the $NbSe_2$. Using the computed values of $|\delta\omega/\delta P|_{(E^1_{2g})}$ and $|\delta\omega/\delta P|_{(A_{1g})}$ in the low *P* range ($P < 840$ μW), measured $z \approx 13$ μm for our bulk $NbSe_2$ crystallite, the thermal conductivity was calculated, where $k_{E^1_{2g}} \approx 0.13$ W/m.K refers to the in-plane mode, and $k_{A_{1g}} \sim 0.07$ W/m.K refers to the out-of-plane mode. It is interesting to note that $k_{E^1_{2g}}$ is almost 2× higher than the $k_{A_{1g}}$, which is well in line with the earlier observation of $\left|\chi_{E^1_{2g}}\right| > 2\times \left|\chi_{A_{1g}}\right|$, highlighting the presence of anisotropy in thermal conductivity

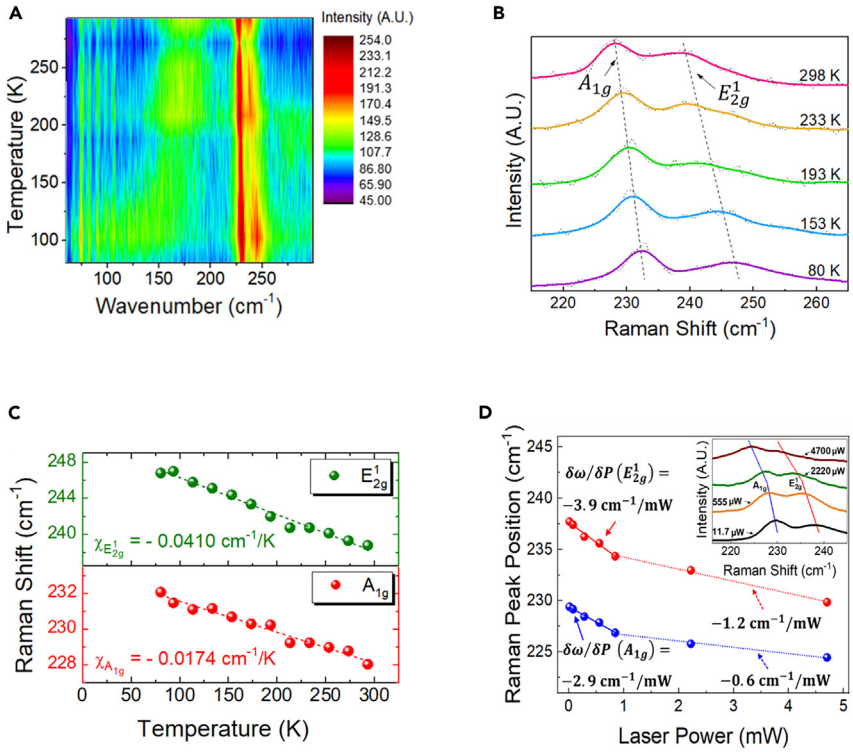

Figure 2. Temperature and excitation laser power dependent Raman spectroscopy of $NbSe_2$

(A) Contour map of the *T*-dependent Raman for 2H-$NbSe_2$ from 80 K to 298 K where the data are collected in 20 K increments at a constant laser *P* of ≈ 0.84 mW.

(B) Stack plot of the Raman spectra of 2H-$NbSe_2$ from 80 K to 298 K. Dashed lines track position of the E^1_{2g} and A_{1g} modes, which exhibits a linear redshift as *T* increases.

(C) Raman shift as a function of *T* for which the $\chi_{E^1_{2g}} \sim -0.041$ cm^{-1}/K and a $\chi_{A_{1g}} \sim -0.0174$ cm^{-1}/K were extracted.

(D) Laser power *P* dependence of the Raman spectra for $NbSe_2$ from ~11.7 μW to ≈ 4700 μW. For laser power $P < 840$ μW, a $\delta\omega/\delta P_{(E^1_{2g})}$ of −3.9 cm^{-1}/mW and $\delta\omega/\delta P_{(A_{1g})}$ of −2.9 cm^{-1}/mW were calculated and a $k_{A_{1g}} \sim 0.07$ W/m.K and $k_{E^1_{2g}} \sim 0.13$ W/m.K was extracted using Equation 3. Variation of $\delta\omega/\delta P$ at higher laser $P > 840$ μW is also plotted as shown by the reduced slope region denoted by the dotted line. The change in slope is attributed to dominance of higher-order *P* coefficient ($[(\delta^2\omega/\delta P^2)P^2]$) which was not addressed in Equation 2 for our computation. We hypothesize that the dominance of ($[(\delta^2\omega/\delta P^2)P^2]$) term in Equation 2 is due to localized heating at $P > 840$ μW. The inset shows the *P*-dependent stack plot of the Raman spectra from 11.7 μW to 4,700 μW, revealing the changed nature of the $\delta\omega/\delta P$ for both the low ($P < 840$ μW) and high slope ($P > 840$ μW) regions in the E^1_{2g} and A_{1g} peak positions.

caused by *T*-dependent and *P*-dependent phonon anharmonicity in the $NbSe_2$. Furthermore, Table 1 summarizes all of the quantitative parameters determined using non-contact Raman spectroscopy on bulk $NbSe_2$ crystallites investigated in our work.

After extensive *T*- and *P*-dependent Raman measurements, the $NbSe_2$ crystallites were once again examined to deduce the possibility of degradation arising from air-exposure or photo-oxidation occurring during these measurements. Thin exfoliated $NbSe_2$ flakes are indeed very sensitive to both air exposure and photo-oxidation. The before and after Raman spectra are shown in Figure S1 (see Supplementary Information) which reveals little shift in the phonon peak positions, indicative of minimal degradation occurring in our samples during the measurements. Incidentally, the phonon peaks of selenium-based 2D materials are reported to shift upon the formation of selenium vacancies, oxygen substitution, or other defects formed through exposure to ambient atmosphere or defect formation through photo-oxidation.[56] However, surface and composition sensitive characterization techniques such as X-ray photoelectron spectroscopy (XPS) would allow further validation of photo-oxidation states in the $NbSe_2$ which may be interesting to explore in a future study. In reviewing the existing literature,[50,57,58] our measurement range is broad over 80 K–298 K for the *T*-dependent Raman, to determine χ and *k* values for bulk $NbSe_2$ crystallites.

Table 1. First-order temperature coefficient and thermal conductivity parameters for $NbSe_2$

	Measured Value	
Material Property	In-plane	Out-of-plane
First-order *T*-coefficient of phonons (χ)	$\lvert\chi_{E^1_{2g}}\rvert \sim 0.0410$ cm^{-1}/K	$\lvert\chi_{A_{1g}}\rvert \sim 0.0174$ cm^{-1}/K
Thermal conductivity (*k*)	$k_{E^1_{2g}} \sim 0.13$ W/m.K	$k_{A_{1g}} \sim 0.07$ W/m.K

A summary of the in-plane and out-of-plane parameters determined using non-contact Raman spectroscopy on bulk $NbSe_2$.

Furthermore, as reported in a prior study,[59] k is strongly dependent on vacancy and defect concentrations. The wide variation in k values found in the literature for the same material has been observed for single layer graphene,[60] and incidentally also for $NbSe_2$,[61] as reported in the prior literature.[41,62,63] Moreover, early studies successfully demonstrated the use of Raman spectroscopy to deduce k in 2D materials including graphene,[60] where the T-dependent and P-dependent phonon peak positions shift as the T changes, from which k is inferred. Using the shift in the optical phonon peak positions which are sensitive to local heating effects (e.g., caused by ambient temperature or laser-power induced heating), the thermal conductivity for 2D materials can be estimated using such a noncontact approach, despite the fact that the Raman-active optical phonons play a minor role in directly conducting heat along the flake. Balandin and co-workers pioneered this approach in 2008,[60] where the T-dependent and P-dependent G-peak position was used to determine k in graphene. We have used the same approach here following similar guidelines, where the E^1_{2g} and A_{1g} mode variations allowed us to compute k for our bulk $NbSe_2$. However, prior work by Zhang et al.[64] has shown modulation of Raman peak positions and their intensities with the choice of substrate for in-plane and out-of-plane phonons modes. The anisotropy in thermal conductivity reported in our work may also be influenced by the interaction of $NbSe_2$ with the substrate. While not within the scope of this paper, future studies elaborating upon thermal conductivity calculations and its anisotropy may be interesting to gather for both supported and suspended $NbSe_2$ to shed insights on the role the substrate plays. Additionally, bulk $NbSe_2$ is less prone to oxidation compared to thin membranes, and thus no additional Raman peaks appeared, for example at $\sim$ 302 cm^{-1} ascribed previously to the presence of Nb_2O_5 formed after laser irradiation.[65]

Electronic transport measurements

Delta-mode instrumentation

The electronic transport measurements on our bulk $NbSe_2$ samples were conducted using a data acquisition system developed in-house to acquire the superconducting transition temperature T_c using the Lakeshore CRX-4K cryogenic probe stage. The schematic of the instrumentation is shown in Figure 3A. One of the ways in which electronic transport measurements on superconductors are carried out is using a commercially available physical property measurement system (PPMS),[11,57] variable T helium cryostat,[41,65] or closed-cycle two-stage pulse tube with helium stage.[66] In this work, we have developed an approach to make such transport measurements with the CRX-4K probe station using a closed cycle helium refrigerator, where optical radiation is coupled to the device under test (DUT), while the transport measurements are made in vacuum using delta-mode technique.

The delta-mode technique uses an ambipolar current source I_s to the DUT which is squared in amplitude to eliminate the Seebeck voltages at the interfaces. Here, electrical connections and adapters from the instrumentation to the DUT result in a Seebeck coefficient mismatch and a large T gradient in our interconnects on the chip. Since the Seebeck voltages remain constant in magnitude and polarity at a fixed T regardless of current source bias, the average voltage is extracted every n cycles at the maximum operating frequency of 12.5 Hz, as denoted in Equation 4.

$$V_{average} = \sum_{i=1}^{n}\left(\frac{V_{a,n} - 2V_{b,n}+V_{c,n}}{4}\right)(-1)^n \quad \text{(Equation 4)}$$

Here, $V_{average}$ is the measured voltage for the channel R calculation; $V_{a,n}$, $V_{b,n}$, and $V_{c,n}$ are used to indicate the alternating maximum and minimum measured voltages at each n delta cycle. An example of this cyclical behavior in current and voltage is shown in Figure 3B for a given ambipolar input $I_s = \pm$ 100 μA, and $V_{measured}$ varies between 13 μV and 17 μV from n = 0 to n = 8 delta cycles, while the output $V_{average}$ = 15 μV was computed from Equation 4, as represented in Figure 3B.

In order to corroborate the superconducting transition temperature T_c data deciphered using the above Kelvin sensing delta-mode approach, a calibration test was conducted with a sputtered Nb film before proceeding to our $NbSe_2$ device measurements. For the calibration test, a thick Nb film was deposited on an oxidized Si substrate with a thermal oxide thickness of 270 nm using DC sputtering, with an Ar flow rate of ∼15 sccm, pressure of ≈ 5 mTorr, and plasma power of ∼50 W once the plasma stabilized. The delta-mode transport measurement parameters for our Nb film were conducted at I_s = 100 μA (magnitude of I_s selected to maximize the S/N ratio), 10 cycles at 12.5 Hz in a T range from 3.88 K to 300 K. Using these parameters, the T_c ($R = 0\ \Omega$) was measured to be 8.49 K using the CRX-4K system which is close to T_c = 9.18 K acquired for the same sample using the PPMS system (Quantum Design, model DynaCool), as shown in Figure 3C. This resulted in an offset of ∼0.69 K in our T_c data for the two approaches, which we mostly attributed to the position of the T sensor in our CRX-4K system to be well below the sample chuck, resulting in some thermal offset from the true reading at the surface of the material.

Bolometer measurements for deducing optical-to-thermal transduction

Superconducting TES bolometers rely on the abrupt change in resistivity induced by minute changes in temperature of the TES from the absorbed energy from optical sources which we now describe in our prototypical bolometers. Incidentally, there have been several reports on electronic transport measurements on $NbSe_2$ crystals mechanically exfoliated and transferred onto pre-patterned electrodes by using a polydimethylsiloxane (PDMS) stamping process and subsequent e-beam lithography to define electrical contacts.[11,57,65] However, there appears to be no prior reported work on the direct probing of as-grown pristine bulk $NbSe_2$ crystallites to access their intrinsic electronic properties free from surface or interfacial residues commonly associated with post-processing and nanofabrication. The aforementioned delta-mode Kelvin sensing technique allowed us to make measurements on the bulk $NbSe_2$ crystallite which was carefully probed with the Lakeshore tungsten probe tips. A pictograph of our set-up is highlighted in Figure 4A-Left, where the DUT is circled within the red dotted line, and expanded

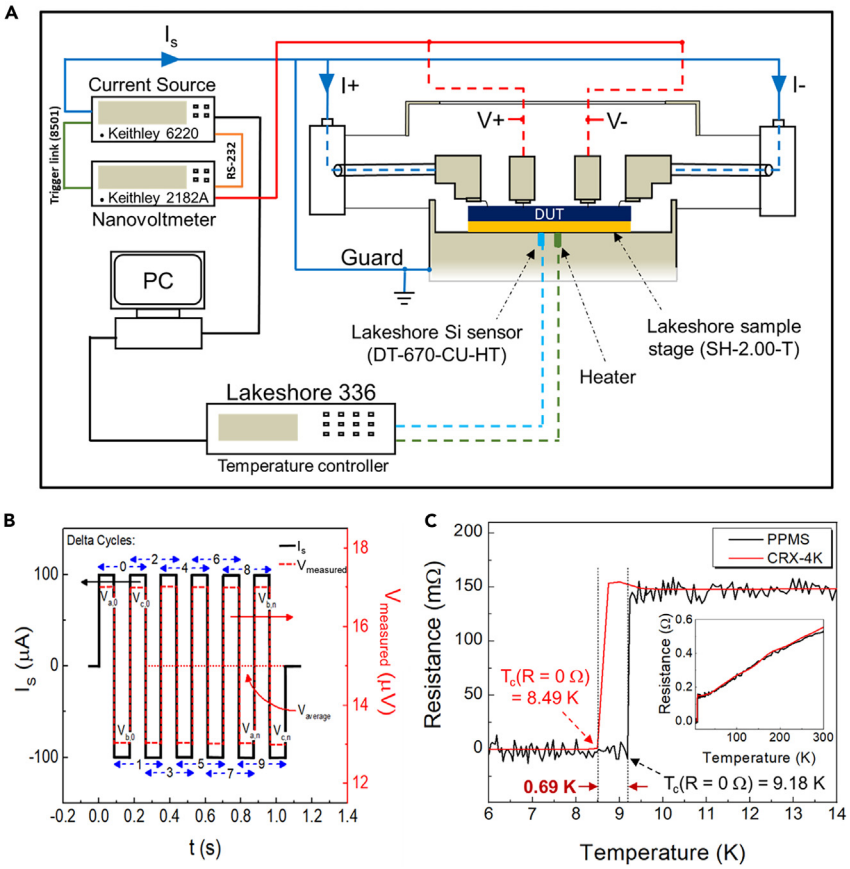

Figure 3. Delta-mode electrical characterization setup for superconducting transition temperature measurement

(A) The instrumentation setup for the electronic transport measurements to determine superconducting T_c using the CRX-4K probe stage. Here, a nanovoltmeter (Keithley 2182A), a precision current source (Keithley 6220), and the Lakeshore 336 temperature controller are interfaced to the CRX-4K probe station, where cooling is achieved using compressed He closed cycle refrigerator.

(B) Input I_s and output V measured from $V+$ to $V-$, as shown in the schematic in (a), at I_s modulated at 12.5 Hz.

(C) The measured R obtained for Nb used as our reference sample for our in-house designed T_c measurement system. The R is plotted as a function of T to tabulate its $T_c(R = 0\ \Omega)$ which occured at 8.49 K in the CRX-4K, while in the PPMS this transition occurs at $T_c(R = 0\ \Omega) = 9.18$ K. The T offset of 0.69 K is attributed to the thermal position of the temperature sensor located well beneath the sample on the SH-2.00-T stage, causing a delta in the actual T on the surface of the sample. The inset shows R as a function of T over a broader T range for the sputtered Nb film from 6 K to 300 K using both the PPMS and the CRX-4K.

on the right inset. The single-mode fiber-coupled (FC) optical sources utilized were the Thorlabs S3FC405 ($\lambda_{405\ nm}$), S1FC660 ($\lambda_{660\ nm}$), and S1FC1060 ($\lambda_{1060\ nm}$), lasers which were interfaced to the CRX-4K fiber-coupled feedthroughs (manufactured by OZ optics) to focus optical radiation onto the DUT at normal incidence, as shown in Figure 4A-left. We mounted the $NbSe_2$ crystal on a single-side polished Si wafer using VGE-7031 thermal varnish; to further improve the thermal contact between the Lakeshore sample stage SH-2.00-T and the DUT, Apiezon N thermal grease was used between the Si wafer and the chuck, as shown by the sample set-up in Figure 4A-Right. We note the several thermal stray paths within the effective thermal circuit illustrated in Figure 4A-right, where an effective thermal conductance G_{eff} and effective thermal capacitance C_{eff} are illustrated for our model system.

Electronic transport measurements were initiated through the previously described delta-mode measurements on $NbSe_2$ crystals from 300 K down to 3.88 K, with $I_s = 1$ mA (magnitude of I_s selected to maximize S/N). Furthermore, when a lower magnitude of $I_s < 100$ μA was used with the current instrumentation, to possibly reduce the effect of Joule heating and decrease the response time, the signal-to-noise ratio in the ensuing I-V was low and the data were noisy, which can be addressed further in future work. Additionally, between consecutive T-dependent measurements, a 300 s equilibration interval was used, to ensure the surface T of $NbSe_2$ ($T_{surface}$) reaches the T set-point denoted as T_{cryo}. Figure 4B shows the $R - T$ behavior at $T_{cryo} < 40$ K, where a $T_c(R = 0\ \Omega)$ was observed at 3.88 K, while the $T_{c,onset}(R = R_n)$ ($R_n \sim 2.6$ mΩ, is the normal state R) was observed at 3.89 K. Moreover, no discernible R hysteresis was found when the DUT was heated and cooled below and above the superconducting transition.

Incidentally, the $T_{c,onset}(R = R_n)$ and T_c $(R = 0\ \Omega)$ noted from our CRX-4K transport measurements are lower than previously reported values of ~6.5 K–7.2 K for bulk $NbSe_2$.[53,54] We believe that the offset in the T_c $(R = 0\ \Omega)$ in our $NbSe_2$ bulk crystallite with the CRX-4K is a result

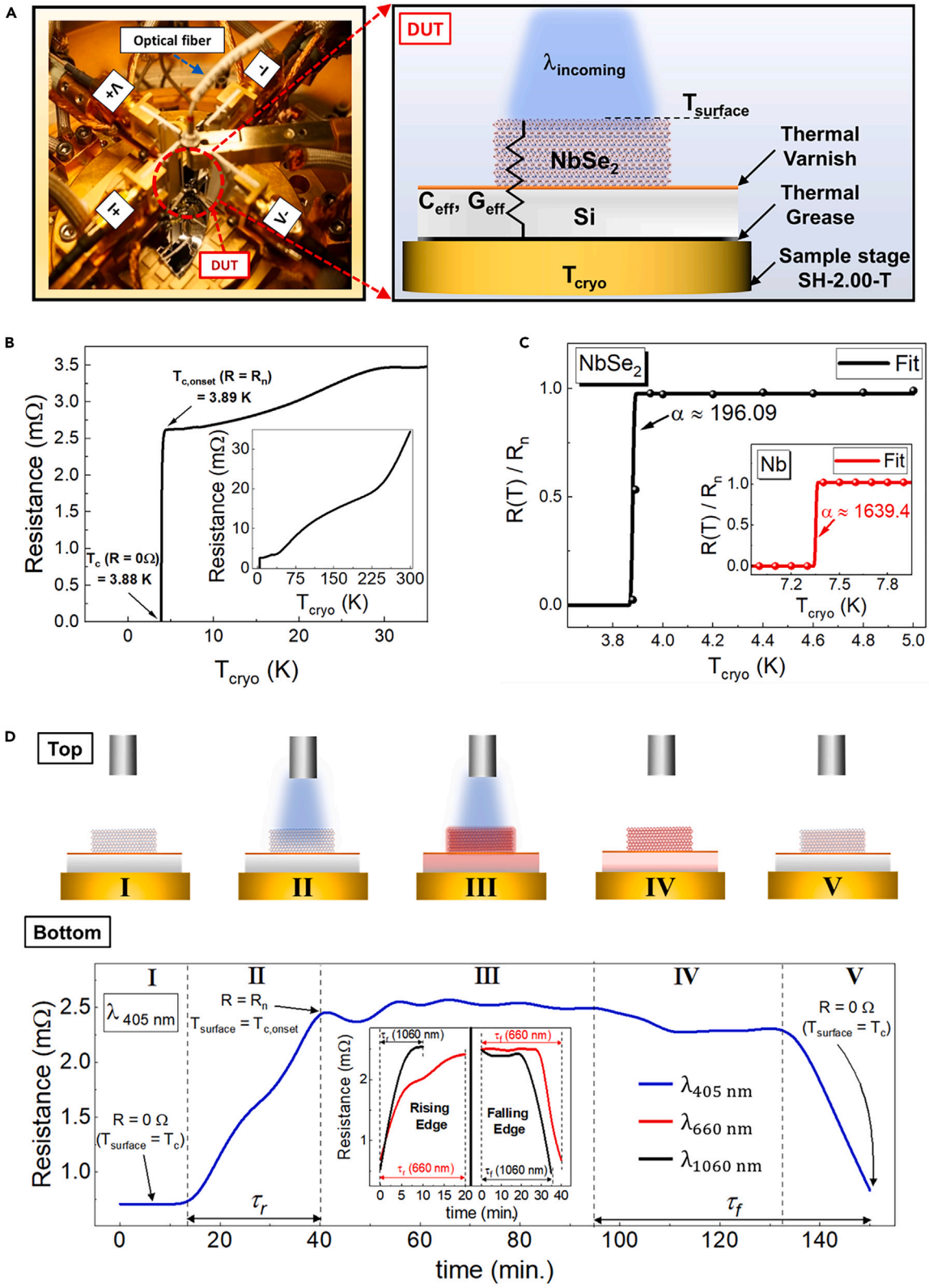
A
Optical fiber
V+
I-
I+
V-
DUT
DUT
λincoming
Tsurface
NbSe2
Ceff, Geff
Si
Tcryo
Thermal Varnish
Thermal Grease
Sample stage SH-2.00-T
B
Tc,onset (R = Rn) = 3.89 K
Tc (R = 0Ω) = 3.88 K
Resistance (mΩ)
Tcryo (K)
C
NbSe2
Fit
α ≈ 196.09
R(T) / Rn
Nb
α ≈ 1639.4
Tcryo (K)
D
Top
I
II
III
IV
V
Bottom
λ 405 nm
R = 0 Ω (Tsurface = Tc)
R = Rn
Tsurface = Tc,onset
τr
τf
Rising Edge
Falling Edge
τr (1060 nm)
τr (660 nm)
τf (660 nm)
τf (1060 nm)
time (min.)
λ405 nm
λ660 nm
λ1060 nm

Figure 4. *in situ* optically induced superconducting transition temperature measurement of $NbSe_2$

(A) Left: a visual of the four-point probing set up used in the CRX-4K cryogenic stage, with the optical fiber and the four terminals for the voltage and current probe connections in the Kelvin-probe set-up. Shown by the dotted-red circle is the DUT which is expanded on the Right. Right: a schematic of our $NbSe_2$ prototypical superconducting bolometer with all the thermal links illustrated until the sample stage SH-2.00-T.

(B) The R is plotted as a function of T_{cryo} from 0 K up to 40 K, revealing the $T_{c,onset}$ ($R = R_n$) occurring at 3.89 K and T_c ($R = 0\ \Omega$) occurs at 3.88 K. Inset shows the R as a function of T over a wider T range from 300 K down to the superconducting transition.

(C) Measured $R(T)/R_n$ and from the approximation fit to the $R(T)/R_n$ data modeled using Equation 5, a unitless transition bandwidth α was computed. Through the NRA approximation, α was determined to be ~196 for $NbSe_2$. Inset shows the measured $R(T)/R_n$ and approximation fit $R(T)/R_n$ for Nb, revealing an α of ~1639.

(D) Time-resolved photo response of $NbSe_2$ where R is plotted as a function of t using an optical source with $\lambda_{405\ nm}$. The plot is divided into five regions (I to V) with respect to the temporal response of the DUT as a function of the wavelength of the incoming laser source. Inset shows the temporal response in the rising edge and falling edge of the DUT with additional irradiation sources at $\lambda_{660\ nm}$ and $\lambda_{1060\ nm}$. Evidently, we observe $\tau_r|_{1060\ nm} < \tau_r|_{660\ nm} < \tau_r|_{405\ nm}$ and $\tau_f|_{1060\ nm} < \tau_f|_{660\ nm} < \tau_f|_{405\ nm}$.

of poor thermal coupling associated with the underlying layers in our DUT to the CRX-4K stage. We have used GE-7031 varnish for thermal coupling of the superconducting crystal with the cryostage, as shown by the schematic in Figure 4A-Right. Our assumption is further corroborated by the data in Figure S2 which shows T_c measurements on the same sample obtained using vibrating sample magnetometry (VSM) within a PPMS. As seen from Figure S2, the onset of $T_c \sim 6.78$ K for this sample, which is in close agreement with previously reported T_c values for bulk $NbSe_2$.[53,54] Additionally, EDS analysis in Figure S3 in the Supplementary Information section, discusses the near stoichiometric ratio of Nb:Se, thus confirming our notion of the lower T_c ($R = 0\ \Omega$) measured with the CRX-4K to be associated with poor coupling of the underlying layers in our DUT to the CRX-4K stage (i.e., GE-7031 varnish). In the case of superconducting thin films that are directly deposited on a substrate using techniques such as physical vapor deposition, this offset in T_c is expected to be smaller given the direct adhesion of the film to the substrate rather than relying on thermal varnish to couple the two. Since the primary objective of our work here was to assess the optically induced superconducting-to-normal-state phase transition in bulk $NbSe_2$, we successfully demonstrate the function of this prototypical bolometer behavior using the CRX-4K. The inset in Figure 4B shows the entire temperature sweep from 300 K down to the superconducting transition, where the residual resistivity ratio (*RRR*) was tabulated to be ~13; the *RRR* in this case was taken as the ratio $R_{300\ K}/R_{8\ K}$ and these data are consistent with a prior report for CVT synthesized $NbSe_2$ crystallites with $RRR \sim 16$.[7]

For our bolometer measurements, the incident laser power P at the sample was calibrated using a Thorlabs PM100D power meter with a silicon photodiode on the SH-2.00-T. The T_{cryo} was maintained at near T_c ($R = 0\ \Omega$) = 3.88 K, and $\lambda_{405\ nm}$, $\lambda_{660\ nm}$, and $\lambda_{1060\ nm}$ optical sources at $P \sim 4.45$ mW were then used at normal incidence to shine electromagnetic radiation on the sample surface, which triggered the switch to the normal state. For irradiating with $\lambda_{405\ nm}$, $\lambda_{660\ nm}$, and $\lambda_{1060\ nm}$, the laser spot was placed between the four probes used to measure resistance of the bulk $NbSe_2$ crystal, as depicted in Figure 4A. The approximate laser spot size was ~250 μm, which is far smaller than the lateral dimensions of the crystal, i.e., 2 mm × 1 mm (length × width). The optical source was thus placed in the middle of the $NbSe_2$ crystal ensuring that the electrically probed region captured the interaction the sample had with the incoming light source. The simplest approximation of the sensitivity of a superconducting absorber layer for TES bolometers is given by a unitless parameter α, which is captured by the following,[67]

$$[R(T)\ /\ R_n] \approx 0.5(tanh(\pi\alpha(T_{surface} - T_c)) + 1) \quad \text{(Equation 5)}$$

Here, $R(T)$ is the R as a function of T, R_n is the normal state resistance at the onset of the superconducting transition, $T_{surface}$ is the temperature at the surface of the $NbSe_2$ under an incoming flux of photons (see Figure 4A-right), and T_c ($R = 0\ \Omega$) = 3.88 K is the superconducting transition temperature of the $NbSe_2$ crystallite. We used the $R - T$ data from Figure 4B and performed a non-linear regression analysis (NRA) to fit Equation 5 to our measured $[R(T)\ /R_n]$ as a function of T_{cryo} between 3.88 K and 5 K, as shown in Figure 4C. We assumed $T_{surface} = T_{cryo}$ in the laser-off condition, and as noted previously a 300 s interval was used in between sampling the R data to equilibrate $T_{surface}$ to the setpoint T_{cryo}. The sensitivity α was computed to be ~196 for our direct-probed bulk $NbSe_2$ (α_{NbSe_2}) using the NRA fitting technique, with the idea to minimize the sum of squared residuals (SSR); here SSR is the sum square deviation between the measured $[R(T)\ /R_n]$ values and the fit approximation of $[R(T)\ /R_n]$ from Equation 5. Similarly, the inset in Figure 4C shows the NRA fit of $[R(T)\ /R_n]$ to our measured $[R(T)\ /R_n]$ for direct probed sputtered Nb film (α_{Nb}), where the α_{Nb} was computed to be ~1639, evidently it was found that $\alpha_{NbSe_2} \ll \alpha_{Nb}$. For our direct-probed superconducting $NbSe_2$, the calculated α signifies good electrothermal feedback, exhibiting higher sensitivity compared to, for example, a typical superconducting thermistors in a TES architecture ($\alpha \sim 10$).[68,69]

Next, we have investigated the λ-dependent optical-to-thermal transduction present in our DUT comprising of the $NbSe_2$ van der Waals crystal. To initiate the temporal and λ-dependent measurements, the modulation of R as a function of time t under $\lambda_{405\ nm}$ illumination was measured and the data are presented in Figure 4D. The fiber coupled laser at $\lambda_{405\ nm}$ was fixed at $P \sim 4.45$ mW and $I_s = 1$ mA was used for the delta-mode measurements of R at 300 s intervals. This yielded a transition from $R = 0\ \Omega|_{T_{surface} = T_c}$ to $R = R_n|_{T_{surface} = T_{c,onset}}$ under the influence of optical irradiation. Five regions of operation are evident denoted as such at the top of Figure 4D, from regions I to V, while the bottom shows the empirically calculated rise time τ_r,which is defined as the time taken by the $NbSe_2$ sensor to heat up and change its resistance from $R = 0\ \Omega|_{T_{surface} = T_c}$ to $R = R_n|_{T_{surface} = T_{c,onset}}$ after the laser source was turned on. Similarly on the falling edge, the fall time τ_f was computed as the time taken for the $NbSe_2$ absorber to transduce from $R = R_n|_{T_{surface} = T_{c,onset}}$ to $R = 0\ \Omega|_{T_{surface} = T_c}$ (i.e., reverting back to the superconducting state), after the laser was turned off. In region I, the DUT was maintained in the superconducting state such that $R = 0\ \Omega|_{T_{surface} = T_c}$, at $T_{cryo} = 3.88$ K, with the laser off. In region II, the laser was turned on, which caused R to increase gradually, eventually resulting in the switch from

$R = 0\ \Omega|_{T_{surface} = T_c}$ to $R = R_n|_{T_{surface} = T_{c,onset}}$. Here, τ_r was empirically measured to be 25 min for the $\lambda_{405\ nm}$ irradiation source on our direct-probed $NbSe_2$ sensor. In region III, with the laser still on, a saturation of $R = R_n|_{T_{surface} = T_{c,onset}}$ came about, as a result of thermal equilibrium between the environment and thermal dissipation to the SH-2.00-T sample stage. For ease of visualization, the increase in T of the bolometer is schematically represented by a broad color change from gray-to-red for the absorber in traversing regions II to III (top panel of Figure 4D). In region IV, the laser is turned off, and there is a dwell time from $R = R_n|_{T_{surface} = T_{c,onset}}$ to $R = 0\ \Omega|_{T_{surface} = T_c}$. Finally, in region V, a thermal phase transduction is evident in going from $R = R_n|_{T_{surface} = T_{c,onset}}$ to $R = 0\ \Omega|_{T_{surface} = T_c}$. Using the data in regions IV and V, τ_f was empirically computed to be 55 min for the $\lambda_{405\ nm}$ source. Furthermore, the inset in the bottom panel of Figure 4D plots the $R - t$ response of the DUT using other irradiation sources, specifically $\lambda_{660\ nm}$ and $\lambda_{1060\ nm}$ where the τ_r and τ_f values were determined empirically. Interestingly, the λ-dependent trend of our DUT's time constants was found to follow $\tau_r|_{1060\ nm}(10\ min.) < \tau_r|_{660\ nm}(20\ min.) < \tau_r|_{405\ nm}(25\ min.)$, and similarly $\tau_f|_{1060\ nm}(35\ min.) < \tau_f|_{660\ nm}(40\ min.) < \tau_f|_{405\ nm}(55\ min.)$, which is now elaborated more upon next.

Increasing λ decreased τ_r, as observed, implying that the higher incident λ value resulted in a faster optical-to-thermal transduction occurring within the $NbSe_2$ TES sensor. We assume that the λ-dependent trend in our DUT's temporal response is related to the λ-dependent reflectivity of the $NbSe_2$ crystallites previously reported by Liang. et al.[70] and Hill. et al.[71] who both noted an increased reflectivity in $NbSe_2$ with a decrease in λ; this is also consistent with our observations for $\lambda_{450\ nm}$ to $\lambda_{1060\ nm}$. We hypothesize that since a higher ratio of the incident electromagnetic radiation is reflected at lower incident λ values, the DUT takes more time to heat up from $R = 0\ \Omega|_{T_{surface} = T_c}$ to $R = R_n|_{T_{surface} = T_{c,onset}}$, leading to our empirical observation that $\tau_r|_{1060\ nm} < \tau_r|_{660\ nm} < \tau_r|_{405\ nm}$. Furthermore, for all the λ values used in this temporal response study, we see that $\tau_f \gg \tau_r$ for our prototypical bolometer. We presume this is associated with the poor heat dissipation from the superconducting $NbSe_2$ layer to the Si thermal heat sink, since there is a 10-fold decrease in Si's thermal conductance at $T_{cryo} < 20$ K compared to that at room T,[72] limiting the thermal coupling to the SH-2.00-T sample stage, in order for the DUT to revert back to the superconducting state. The τ_r and τ_f recorded with the DUT under the optical stimulus is unmistakably linked to the thermal conductivities $k_{E^1_{2g}}$ and $k_{A_{1g}}$ of the bulk $NbSe_2$ evaluated through Raman spectroscopic analyses presented here. However, the response of the system is the sum of the thermal conductivities of the several layers such as Si, thermal grease, thermal varnish and the $NbSe_2$, as described in Figure 4A. To reiterate, the primary focus of this work was to provide a proof-of-concept demonstration of the $NbSe_2$ to optical irradiation in a TES architecture. The emphasis of this study was to highlight the prototypical demonstration of bulk $NbSe_2$ highlighting a transduction from $R = 0\ \Omega|_{T_{surface} = T_c}$ to $R = R_n|_{T_{surface} = T_{c,onset}}$ by optical stimulation, using the proposed equipment setup. Our study was not motivated by benchmarking because it is heavily dependent on the architecture of the DUT, and the defect concentration in the crystallite, as discussed earlier in this paper. The thermal conductivity of $NbSe_2$ obtained through Raman spectroscopy can be extended to other material systems for determining thermal conductivities using non-contact approaches. Furthermore, the effective heat capacitance C_{eff} is inversely dependent on k, where higher C_{eff} values are correlated to a lower thermal noise within the TES device.[67] This implies that the anisotropy in k values for $NbSe_2$ reported in our study may perhaps be used to deduce $NbSe_2$ crystal's orientation to optimize thermal noise performance. In the case when $NbSe_2$ is suspended, the C_{eff} of the TES maybe further reduced to improve thermal noise performance.

For TES measurements, an alternative unambiguous approach for determining the modulation of $T_c\ (R = 0\ \Omega)$ to $T_{c,onset}(R = R_n)$ under the influence of optical irradiation maybe possible by extracting DC *I-V* curves to measure the critical current density and extracting the superconducting energy gap of bulk $NbSe_2$,[73,74] as part of a future study. Moreover, our work focuses on analyzing the intrinsic electrical response of $NbSe_2$ biased at its superconducting state, such that with incident optical stimulation, it causes it to switch to the normal state with the proof-of-concept validation of the $NbSe_2$ crystal as a TES. $NbSe_2$ in its 2D form <10 layers, has also shown evidence of superconductivity but the transition temperature appears to decrease as sample thickness decreases.[37] While our samples were bulk, the findings of this study can easily be translated to thinner films of $NbSe_2$ approaching the 2D limit. Furthermore, another degree of freedom is afforded in 2D $NbSe_2$ to modulate its transition temperature through the thickness dependent dielectric screening that decreases as the sample thickness decreases for <10 layers. This allows external electric or magnetic fields to couple to the dielectric environment which changes with thickness, as reported previously.[38,75]

DISCUSSION

In this work, a comprehensive characterization of single-crystalline $NbSe_2$ was conducted toward a prototypical TES bolometer demonstration. A superconducting transition in bulk $NbSe_2$ was determined to occur at ~ 3.88 K using the delta-mode Kelvin sensing technique by direct electrical probing in a Lakeshore CRX-4K probe stage. Several optical radiation sources from the UV-to-IR ($\lambda_{405\ nm}$, $\lambda_{660\ nm}$ and $\lambda_{1060\ nm}$) were used to determine various operational parameters of our sensors. The bolometer's switching time constants showed a λ-dependent temporal response; for example, the rising time constant showed the following sequence: $\tau_r|_{1060\ nm} < \tau_r|_{660\ nm} < \tau_r|_{405\ nm}$. The λ-dependent trend in our DUT's temporal response is attributed to the λ-dependent reflectivity of the $NbSe_2$ crystallites, as explained in the Results section. The temperature and laser power dependent Raman spectroscopy analysis revealed a directional anisotropy in thermal conductivity k, where, $k_{E^1_{2g}} \sim 0.13$ W/m.K and $k_{A_{1g}} \sim 0.07$ W/m.K was computed, suggesting $k_{E^1_{2g}} \sim 2\times\ k_{A_{1g}}$, presumably due to phonon anharmonicity. This work shows a proof-of-concept demonstration of $NbSe_2$ where a transduction from its zero-state resistance to normal-state resistance is evident through optical stimulation and indicates the promise of 2D $NbSe_2$ toward future TES devices and bolometers. These devices maybe further miniaturized through lithographic patterning in the future, for the realization of monolithically integrated sensors which may be coupled to rf, microwave, and quantum photonic components.

Limitations of the study

Surface and composition-sensitive characterization methods, such as X-ray photoelectron spectroscopy (XPS), may allow for additional confirmation of photo-oxidation states in $NbSe_2$, which may be worth investigating in future work. The interaction of $NbSe_2$ with the substrate may potentially have an effect on the anisotropy in thermal conductivity revealed in our study. Additional research into thermal conductivity calculations and anisotropy for both supported and suspended $NbSe_2$ may thus be useful in shedding insights into the role the substrate itself plays. The current investigation on bulk $NbSe_2$ used in this work should serve as a benchmark for future extensions of this empirical study to validate theoretically predicted phenomena for TES devices based on $NbSe_2$ in the limit of monolayers and extracting thickness-dependent device parameters.

RESOURCE AVAILABILITY

Lead contact

Futher information and requests for resources should be directed to the lead contact, Anupama Kaul (Anupama.Kaul@unt.edu).

Material availability

This study did not generate any new materials.

Data and code availability

- All data reported in this paper will be shared by the lead contact upon request.
- This paper does not report original code.
- Any additional information required to reanalyze the data reported in this paper is available from the lead contact upon request.

ACKNOWLEDGMENTS

We thank the Air Force Office of Scientific Research (grant number FA9550-15-1-0200 and FA9550-21-1-0404), the National Science Foundation (grant number NSF ECCS 1753933) and the US Department of Energy (grant number DE-NA0004114) who provided funding support that enabled us to pursue this work. G.K. acknowledges support from the US Department of Energy (grant number DE-FOA-0002514). S.K. and A.V.D. acknowledge support through the Materials Genome Initiative funding allocated to the National Institute of Standards and Technology.

AUTHOR CONTRIBUTIONS

A.B.K. conceived the overall project. K. J and G. A. S. conducted the experiments related to instrumentation set-up and transport and material characterization. S. K. and A. V. D. synthesized the 2D crystals. G. K. and S. K. conducted the material characterization studies, Z. L. and W. Z. assisted in the device fabrication and measurements. All contributed to discussions related to figure edits. A.B.K. and K. J. analyzed the data, conducted significant manuscript edits and came up with the conclusions. All reviewed the manuscript writing and approved of its content.

DECLARATION OF INTERESTS

The authors declare no competing interests.

STAR★METHODS

Detailed methods are provided in the online version of this paper and include the following:

SUPPLEMENTAL INFORMATION

Supplemental information can be found online at https://doi.org/10.1016/j.isci.2024.110818.

Received: March 10, 2024
Revised: July 30, 2024
Accepted: August 22, 2024
Published: August 26, 2024

REFERENCES

1. Novoselov, K.S., Jiang, D., Schedin, F., Booth, T.J., Khotkevich, V.V., Morozov, S.V., and Geim, A.K. (2005). Two-dimensional atomic crystals. Proc. Natl. Acad. Sci. USA *102*, 10451–10453. https://doi.org/10.1073/pnas.0502848102.
2. Zhang, X., Tan, Q.-H., Wu, J.-B., Shi, W., and Tan, P.-H. (2016). Review on the Raman spectroscopy of different types of layered materials. Nanoscale *8*, 6435–6450. https://doi.org/10.1039/C5NR07205K.
3. Xia, F., Wang, H., Xiao, D., Dubey, M., and Ramasubramaniam, A. (2014). Two-dimensional material nanophotonics. Nat. Photonics *8*, 899–907. https://doi.org/10.1038/nphoton.2014.271.
4. Min, M., Sakri, S., Saenz, G.A., and Kaul, A.B. (2021). Photophysical Dynamics in Semiconducting Graphene Quantum Dots Integrated with 2D MoS2 for Optical Enhancement in the Near UV. ACS Appl. Mater. Interfaces *13*, 5379–5389. https://doi.org/10.1021/acsami.0c18615.
5. Jayanand, K., Chugh, S., Adhikari, N., Min, M., Echegoyen, L., and Kaul, A.B. (2020). Sc_3N@C80 and La@C82 doped graphene for a new class of optoelectronic devices. J. Mater. Chem. C *8*, 3970–3981.
6. Bandyopadhyay, A.S., Adhikari, N., and Kaul, A.B. (2019). Quantum Multibody Interactions in Halide-Assisted Vapor-Synthesized Monolayer WSe_2 and Its Integration in a High Responsivity Photodetector with Low-Interface Trap Density. Chem. Mater. *31*, 9861–9874. https://doi.org/10.1021/acs.chemmater.9b04086.
7. Frindt, R.F. (1972). Superconductivity in Ultrathin $NbSe_2$ Layers. Phys. Rev. Lett. *28*, 299–301.
8. Kaul, A.B. (2014). Two-dimensional layered materials: Structure, properties, and prospects for device applications. J. Mater. Res. *29*, 348–361. https://doi.org/10.1557/jmr.2014.6.
9. Mak, K.F., Lee, C., Hone, J., Shan, J., and Heinz, T.F. (2010). Atomically thin MoS_2: A new direct-gap semiconductor. Phys. Rev. Lett. *105*, 2–5. https://doi.org/10.1103/PhysRevLett.105.136805.
10. Wilson, J.A., Di Salvo, F.J., and Mahajan, S. (2001). Charge-density waves and superlattices in the metallic layered transition metal dichalcogenides. Adv. Phys. X. *50*, 1171–1248. https://doi.org/10.1080/00018730110102718.
11. Xing, Y., Zhao, K., Shan, P., Zheng, F., Zhang, Y., Fu, H., Liu, Y., Tian, M., Xi, C., Liu, H., et al. (2017). Ising superconductivity and quantum phase transition in macro-size monolayer $NbSe_2$. Nano Lett. *17*, 6802–6807. https://doi.org/10.1021/acs.nanolett.7b03026.
12. Josephson, B.D. (1962). Possible new effects in superconductive tunnelling. Phys. Lett. *1*, 251–253. https://doi.org/10.1016/0031-9163(62)91369-0.
13. Martinis, J.M., Devoret, M.H., and Clarke, J. (2020). Quantum Josephson junction circuits and the dawn of artificial atoms. Nat. Phys. *16*, 234–237. https://doi.org/10.1038/s41567-020-0829-5.
14. Kaul, A.B., Whiteley, S.R., Van Duzer, T., Yu, L., Newman, N., and Rowell, J.M. (2001). Internally shunted sputtered NbN Josephson junctions with a TaNx barrier for nonlatching logic applications. Appl. Phys. Lett. *78*, 99–101. https://doi.org/10.1063/1.1337630.
15. Kaul, A.B., Bumble, B., Lee, K.A., LeDuc, H.G., Rice, F., and Zmuidzinas, J. (2004). Fabrication of wide-IF 200-300 GHz superconductor-insulator-superconductor mixers with suspended metal beam leads formed on silicon-on-insulator. J. Vac. Sci. Technol. B Microelectron. Nanom. Struct. *22*, 2417–2422. https://doi.org/10.1116/1.1798831.
16. Harris, R., Johnson, M.W., Han, S., Berkley, A.J., Johansson, J., Bunyk, P., Ladizinsky, E., Govorkov, S., Thom, M.C., Uchaikin, S., et al. (2008). Probing noise in flux qubits via macroscopic resonant tunneling. Phys. Rev. Lett. *101*, 117003. https://doi.org/10.1103/PhysRevLett.101.117003.
17. Wang, H., Guo, J., Miao, J., Luo, W., Gu, Y., Xie, R., Wang, F., Zhang, L., Wang, P., and Hu, W. (2022). Emerging Single-Photon Detectors Based on Low-Dimensional Materials. Small *18*, 2103963. https://doi.org/10.1002/smll.202103963.
18. Zmuidzinas, J., and Richards, P.L. (2004). Superconducting detectors and mixers for millimeter and submillimeter astrophysics. Proc. IEEE *92*, 1597–1616. https://doi.org/10.1109/JPROC.2004.833670.
19. Bacrania, M.K., Hoover, A.S., Karpius, P.J., Rabin, M.W., Rudy, C.R., Vo, D.T., Beall, J.A., Bennett, D.A., Doriese, W.B., Hilton, G.C., et al. (2009). Large-area microcalorimeter detectors for ultra-high-resolution x-ray and gamma-ray spectroscopy. IEEE Trans. Nucl. Sci. *56*, 2299–2302.
20. Irwin, K.D. (1995). An application of electrothermal feedback for high resolution cryogenic particle detection. Appl. Phys. Lett. *66*, 1998–2000. https://doi.org/10.1063/1.113674.
21. Hadfield, R.H., and Johansson, G. (2016). Superconducting Devices in Quantum Optics (Springer International Publishing), pp. 31–60. https://doi.org/10.1007/978-3-319-24091-6.
22. Giustina, M., Versteegh, M.A.M., Wengerowsky, S., Handsteiner, J., Hochrainer, A., Phelan, K., Steinlechner, F., Kofler, J., Larsson, J.Å., Abellán, C., et al. (2015). Significant-Loophole-Free Test of Bell's Theorem with Entangled Photons. Phys. Rev. Lett. *115*, 250401. https://doi.org/10.1103/PhysRevLett.115.250401.
23. den Hartog, R., Barret, D., Gottardi, L., den Herder, J.-W., Jackson, B., de Korte, P., van der Kuur, J., van Leeuwen, B.-J., van Loon, D., and Nieuwenhuizen, A. (2014). Requirements for the detectors and read-out of ATHENA X-IFU. In Space Telescopes and Instrumentation 2014: Ultraviolet to Gamma Ray (International Society for Optics and Photonics), p. 91445Q. https://doi.org/10.15407/spqeo15.03.193.
24. Ruhl, J., Ade, P.A.R., Carlstrom, J.E., Cho, H.-M., Crawford, T., Dobbs, M., Greer, C.H., Halverson, N.w., Holzapfel, W.L., Lanting, T.M., et al. (2004). The South Pole Telescope. In Proc.SPIE, *5498*Proc.SPIE (SPIE), pp. 11–29. https://doi.org/10.1117/12.552473.
25. Betancourt-Martinez, G.L., Adams, J., Bandler, S., Beiersdorfer, P., Brown, G., Chervenak, J., Doriese, R., Eckart, M., Irwin, K., and Kelley, R. (2014). The transition-edge EBIT microcalorimeter spectrometer. In Space Telescopes and Instrumentation 2014: Ultraviolet to Gamma Ray (International Society for Optics and Photonics), p. 91443U.
26. De Graauw, T., Helmich, F.P., Phillips, T.G., Stutzki, J., Caux, E., Whyborn, N.D., Dieleman, P., Roelfsema, P.R., Aarts, H., Assendorp, R., et al. (2010). The Herschel-heterodyne instrument for the far-infrared (HIFI). Astron. Astrophys. *518*, L6.
27. Zmuidzinas, J. (2012). Superconducting Microresonators: Physics and Applications. Annu. Rev. Condens. Matter Phys. *3*, 169–214. https://doi.org/10.1146/annurev-conmatphys-020911-125022.
28. Polakovic, T., Armstrong, W., Karapetrov, G., Meziani, Z.-E., and Novosad, V. (2020). Unconventional Applications of Superconducting Nanowire Single Photon Detectors. Nanomaterials *10*, 1198. https://doi.org/10.3390/nano10061198.
29. Bock, J., Day, P., Goldin, A., LeDuc, H.G., Hunt, C., Lange, A., Vayonakis, A., and Zmuidzinas, J. (2002). Antenna-coupled bolometer array for astrophysics. In Proc. Far-IR, Sub-MM, MM Detect. Work, pp. 224–229.
30. Richards, P.L. (1994). Bolometers for infrared and millimeter waves. J. Appl. Phys. *76*, 1–24. https://doi.org/10.1063/1.357128.
31. Morozov, D.V., Casaburi, A., and Hadfield, R.H. (2021). Superconducting photon detectors. Contemp. Phys. *62*, 69–91. https://doi.org/10.1080/00107514.2022.2043596.
32. Bleem, L., Ade, P., Aird, K., Austermann, J., Beall, J., Becker, D., Benson, B., Britton, J., Carlstrom, J., Chang, C.L., et al. (2012). An Overview of the SPTpol Experiment. J. Low Temp. Phys. *167*, 859–864. https://doi.org/10.1007/s10909-012-0505-y.
33. Gershenzon, E.M., Gol'Tsman, G.N., Gousev, Y.P., Elant'ev, A.I., and Semenov, A.D. (1991). Electromagnetic radiation mixer based on electron heating in resistive state of superconductive Nb and YBaCuO films. IEEE Trans. Magn. *27*, 1317–1320.
34. Gol'tsman, G.N., Karasik, B.S., Okunev, O.V., Dzardanov, A.L., Gershenzon, E.M., Ekstrom, H., Jacobsson, S., and Kollberg, E. (1995). NbN hot electron superconducting mixers for 100 GHz operation. IEEE Trans. Appl. Supercond. *5*, 3065–3068.
35. Raasch, J., Szwaj, C., Thoma, P., Zen, H., Konomi, T., Scheuring, A., Siegel, M., Ilin, K., Hosaka, M., and Holzapfel, B. (2014). Electrical field sensitive high-Tc YBCO detector for real-time observation of CSR. In Proc. IPAC, pp. 1–4.
36. Bevilacqua, S., Novoselov, E., Cherednichenko, S., Shibata, H., and Tokura, Y. (2014). MgB_2 Hot-Electron Bolometer Mixers at Terahertz Frequencies. IEEE Trans. Appl. Supercond. *25*, 1–4.
37. de la Barrera, S.C., Sinko, M.R., Gopalan, D.P., Sivadas, N., Seyler, K.L., Watanabe, K., Taniguchi, T., Tsen, A.W., Xu, X., Xiao, D., and Hunt, B.M. (2018). Tuning Ising superconductivity with layer and spin–orbit coupling in two-dimensional transition-metal dichalcogenides. Nat. Commun. *9*, 1427. https://doi.org/10.1038/s41467-018-03888-4.
38. Xi, X., Berger, H., Forró, L., Shan, J., and Mak, K.F. (2016). Gate Tuning of Electronic Phase Transitions in Two-Dimensional ${\mathrm {NbSe}}_{2. Phys. Rev. Lett. *117*, 106801. https://doi.org/10.1103/PhysRevLett.117.106801.
39. Choi, S.H., Yun, S.J., Won, Y.S., Oh, C.S., Kim, S.M., Kim, K.K., and Lee, Y.H. (2022). Large-scale synthesis of graphene and other 2D materials towards industrialization. Nat. Commun. *13*, 1484. https://doi.org/10.1038/s41467-022-29182-y.

40. Shen, P.-C., Lin, Y., Wang, H., Park, J.-H., Leong, W.S., Lu, A.-Y., Palacios, T., and Kong, J. (2018). CVD Technology for 2-D Materials. IEEE Trans. Electron. Dev. *65*, 4040–4052. https://doi.org/10.1109/TED.2018.2866390.
41. Wang, H., Huang, X., Lin, J., Cui, J., Chen, Y., Zhu, C., Liu, F., Zeng, Q., Zhou, J., Yu, P., et al. (2017). High-quality monolayer superconductor $NbSe_2$ grown by chemical vapour deposition. Nat. Commun. *8*, 394–398. https://doi.org/10.1038/s41467-017-00427-5.
42. Lin, H., Chang, M., Fu, X., Li, P., Chen, M., Wu, L., Yang, F., and Zhang, Q. (2023). Tunability of the Superconductivity of NbSe(2) Films Grown by Two-Step Vapor Deposition. Molecules *28*, 1059. https://doi.org/10.3390/molecules28031059.
43. Zou, Y.-C., Chen, Z.-G., Zhang, E., Xiu, F., Matsumura, S., Yang, L., Hong, M., and Zou, J. (2017). Superconductivity and magnetotransport of single-crystalline NbSe2 nanoplates grown by chemical vapour deposition. Nanoscale *9*, 16591–16595. https://doi.org/10.1039/C7NR06617A.
44. Lide, D.R. (2004). CRC Handbook of Chemistry and Physics (CRC press).
45. Mkrtchyan, V., Kumar, R., White, M., Yanxon, H., and Cornelius, A. (2018). Effect of pressure on crystal structure and superconductivity of NbSexTe2−x (x = 2, 1.5). Chem. Phys. Lett. *692*, 249–252. https://doi.org/10.1016/j.cplett.2017.12.042.
46. Hopcroft, M.A., Nix, W.D., and Kenny, T.W. (2010). What is the Young's Modulus of Silicon? J. Microelectromech. Syst. *19*, 229–238. https://doi.org/10.1109/JMEMS.2009.2039697.
47. Wilson, J.A., and Yoffe, A.D. (1969). The transition metal dichalcogenides discussion and interpretation of the observed optical, electrical and structural properties. Adv. Phys. X. *18*, 193–335. https://doi.org/10.1080/00018736900101307.
48. Xi, X., Wang, Z., Zhao, W., Park, J.-H., Law, K.T., Berger, H., Forró, L., Shan, J., and Mak, K.F. (2016). Ising pairing in superconducting NbSe2 atomic layers. Nat. Phys. *12*, 139–143. https://doi.org/10.1038/nphys3538.
49. Pereira, C.M., and Liang, W.Y. (1982). Raman studies of the normal phase of 2H-$NbSe_2$. J. Phys. C Solid State Phys. *15*, L991–L995. https://doi.org/10.1088/0022-3719/15/27/009.
50. Hill, H.M., Rigosi, A.F., Krylyuk, S., Tian, J., Nguyen, N.V., Davydov, A.V., Newell, D.B., and Walker, A.R.H. (2018). Comprehensive optical characterization of atomically thin NbSe2. Phys. Rev. B *98*, 165109. https://doi.org/10.1103/PhysRevB.98.165109.
51. Tsang, J.C., Smith, J.E., and Shafer, M.W. (1976). Raman Spectroscopy of Soft Modes at the Charge-Density-Wave Phase Transition in 2H-NbSe2. Phys. Rev. Lett. *37*, 1407–1410. https://doi.org/10.1103/PhysRevLett.37.1407.
52. Pawbake, A.S., Pawar, M.S., Jadkar, S.R., and Late, D.J. (2016). Large area chemical vapor deposition of monolayer transition metal dichalcogenides and their temperature dependent Raman spectroscopy studies. Nanoscale *8*, 3008–3018.
53. Herchen, H., and Cappelli, M.A. (1991). First-order Raman spectrum of diamond at high temperatures. Phys. Rev. B *43*, 11740–11744. https://doi.org/10.1103/PhysRevB.43.11740.
54. Huang, X., Gao, Y., Yang, T., Ren, W., Cheng, H.-M., and Lai, T. (2016). Quantitative Analysis of Temperature Dependence of Raman shift of monolayer WS2. Sci. Rep. *6*, 32236. https://doi.org/10.1038/srep32236.
55. Sahoo, S., Gaur, A.P.S., Ahmadi, M., Guinel, M.J.F., and Katiyar, R.S. (2013). Temperature-dependent Raman studies and thermal conductivity of few-layer MoS_2. J. Phys. Chem. C *117*, 9042–9047. https://doi.org/10.1021/jp402509w.
56. Lioi, D.B., Gosztola, D.J., Wiederrecht, G.P., and Karapetrov, G. (2017). Photon-induced selenium migration in TiSe2. Appl. Phys. Lett. *110*, 81901.
57. Xi, X., Zhao, L., Wang, Z., Berger, H., Forró, L., Shan, J., and Mak, K.F. (2015). Strongly enhanced charge-density-wave order in monolayer $NbSe_2$. Nat. Nanotechnol. *10*, 765–769. https://doi.org/10.1038/nnano.2015.143.
58. Méasson, M.-A., Gallais, Y., Cazayous, M., Clair, B., Rodière, P., Cario, L., and Sacuto, A. (2014). Amplitude Higgs mode in the $2H\ensuremath{-}{\text{NbSe}}_{2}$ superconductor. Phys. Rev. B *89*, 60503. https://doi.org/10.1103/PhysRevB.89.060503.
59. Che, J., Çagin, T., and Goddard, W.A., III (2000). Thermal conductivity of carbon nanotubes. Nanotechnology *11*, 65–69. https://doi.org/10.1088/0957-4484/11/2/305.
60. Balandin, A.A., Ghosh, S., Bao, W., Calizo, I., Teweldebrhan, D., Miao, F., and Lau, C.N. (2008). Superior Thermal Conductivity of Single-Layer Graphene. Nano Lett. *8*, 902–907. https://doi.org/10.1021/nl0731872.
61. Roeske, F., Shanks, H.R., and Finnemore, D.K. (1977). Superconducting- and normal-state thermal conductivity of Nb${\mathrm{Se}}_{2. Phys. Rev. B *16*, 3929–3935. https://doi.org/10.1103/PhysRevB.16.3929.
62. Nguyen, L., Komsa, H.-P., Khestanova, E., Kashtiban, R.J., Peters, J.J.P., Lawlor, S., Sanchez, A.M., Sloan, J., Gorbachev, R.V., Grigorieva, I.V., et al. (2017). Atomic Defects and Doping of Monolayer NbSe2. ACS Nano *11*, 2894–2904. https://doi.org/10.1021/acsnano.6b08036.
63. Li, Z., Xi, X., Ding, B., Li, H., Liu, E., Yao, Y., and Wang, W. (2020). Thermodynamics and Kinetics Synergy for Controlled Synthesis of 2D van der Waals Single-Crystal NbSe2 via Modified Chemical Vapor Transport. Cryst. Growth Des. *20*, 706–712. https://doi.org/10.1021/acs.cgd.9b01131.
64. Zhang, X., Qiao, X.-F., Shi, W., Wu, J.-B., Jiang, D.-S., and Tan, P.-H. (2015). Phonon and Raman scattering of two-dimensional transition metal dichalcogenides from monolayer{,} multilayer to bulk material. Chem. Soc. Rev. *44*, 2757–2785. https://doi.org/10.1039/C4CS00282B.
65. El-Bana, M.S., Wolverson, D., Russo, S., Balakrishnan, G., Paul, D.M., and Bending, S.J. (2013). Superconductivity in two-dimensional $NbSe_2$ field effect transistors. Supercond. Sci. Technol. *26*, 125020. https://doi.org/10.1088/0953-2048/26/12/125020.
66. Orchin, G.J., De Fazio, D., Di Bernardo, A., Hamer, M., Yoon, D., Cadore, A.R., Goykhman, I., Watanabe, K., Taniguchi, T., Robinson, J.W.A., et al. (2019). Niobium diselenide superconducting photodetectors. Appl. Phys. Lett. *114*, 251103. https://doi.org/10.1063/1.5097389.
67. Benford, D.J., Chervenak, J.A., Irwin, K.D., Moseley Jr, S.H., Shafer, R.A., Staguhn, J.G., and Wollack, E. (2003). Superconducting Bolometer Array Architectures. Millim. Submillim. Detect. Astron. *4855*, 148. https://doi.org/10.1117/12.459423.
68. Lolli, L., Taralli, E., Portesi, C., Rajteri, M., and Monticone, E. (2016). Aluminum–Titanium Bilayer for Near-Infrared Transition Edge Sensors. Sensors *16*, 953. https://doi.org/10.3390/s16070953.
69. Nagler, P.C., Sadleir, J.E., and Wollack, E.J. (2021). Transition-edge sensor detectors for the Origins Space Telescope. J. Astronomical Telesc. Instrum. Syst. *7*, 1–18. https://doi.org/10.1117/1.JATIS.7.1.011005.
70. Liang, W.Y. (1973). Optical anisotropy in layer compounds. J. Phys. C Solid State Phys. *6*, 551–565. https://doi.org/10.1088/0022-3719/6/3/018.
71. Hill, H.M., Rigosi, A.F., Krylyuk, S., Tian, J., Nguyen, N.V., Davydov, A.V., Newell, D.B., and Walker, A.R.H. (2018). Comprehensive optical characterization of atomically thin $NbSe_2$. Phys. Rev. B *98*, 165109. https://doi.org/10.1103/PhysRevB.98.165109.
72. Thompson, J.C., and Younglove, B.A. (1961). Thermal conductivity of silicon at low temperatures. J. Phys. Chem. Solid. *20*, 146–149. https://doi.org/10.1016/0022-3697(61)90146-9.
73. Dvir, T., Massee, F., Attias, L., Khodas, M., Aprili, M., Quay, C.H.L., and Steinberg, H. (2018). Spectroscopy of bulk and few-layer superconducting NbSe2 with van der Waals tunnel junctions. Nat. Commun. *9*, 598. https://doi.org/10.1038/s41467-018-03000-w.
74. Khestanova, E., Birkbeck, J., Zhu, M., Cao, Y., Yu, G.L., Ghazaryan, D., Yin, J., Berger, H., Forró, L., Taniguchi, T., et al. (2018). Unusual Suppression of the Superconducting Energy Gap and Critical Temperature in Atomically Thin NbSe2. Nano Lett. *18*, 2623–2629. https://doi.org/10.1021/acs.nanolett.8b00443.
75. Lin, H., Zhu, Q., Shu, D., Lin, D., Xu, J., Huang, X., Shi, W., Xi, X., Wang, J., and Gao, L. (2019). Growth of environmentally stable transition metal selenide films. Nat. Mater. *18*, 602–607. https://doi.org/10.1038/s41563-019-0321-8.

STAR★METHODS

KEY RESOURCES TABLE

REAGENT or RESOURCE	SOURCE	IDENTIFIER
Chemicals		
Nb powder (99%)	Strem Chemicals	https://www.strem.com/
Se powder (99.999%)	Strem Chemicals	https://www.strem.com/
Software and algorithms		
XRD data Analysis - Jade 6.5 software	Materials Data Inc (MDI)	https://materialsdata.com/
Data analysis and plotting – Origin	OriginLab Corporation	https://www.originlab.com/
Other		
Bruker D8 X-ray diffractometer	Bruker	https://www.bruker.com/en.html
Horiba LabRAM HR Evolution	Horiba Scientific	https://www.horiba.com/int/scientific/
Delta-mode measurement, Keithley 2182A and Keithley 6220	Tektronix	https://www.tek.com/en/products/keithley
Lakeshore CRX-4K	LakeShore Cryotronics	https://www.lakeshore.com/home
Quantum Design Physical Property Measurement System	Quantum Design	https://www.qdusa.com/index.html
Thermo Fisher Apreo 2S Lo Vac Scanning Electron Microscope	Thermo Fisher Scientific	https://www.thermofisher.com/us/en/home.html

EXPERIMENTAL MODEL AND STUDY PARTICIPANT DETAILS

There are no experimental model and study participants to include in this study.

METHOD DETAILS

Growth of $NbSe_2$ crystallites

Polycrystalline $NbSe_2$ was synthesized during a 72-h reaction between stoichiometric amounts of Nb (99.9%, Strem Chemicals) and Se (99.999%, Strem Chemicals) powders in a vacuum-sealed quartz ampoules at 850°C. The quartz ampoules contained ~1 g of polycrystalline $NbSe_2$ charge and ~110 mg (5 mg/cm^3) of $SeBr_4$, which were sealed under vacuum and placed in a single-zone furnace. The T at the charge and crystal growth zones (T_{hot} – T_{cold}) were 825°C–700°C for a growth duration of ~160 h.

X-Ray diffraction and Raman characterization of the $NbSe_2$ crystal

Powder X-ray diffraction (XRD) scans were produced using a Bruker D8 X-ray diffractometer. Materials Data Inc (MDI) Jade 6.5 software (Livermore, CA 2015) was used to calculate the lattice parameters. The micro-Raman spectroscopy measurements were carried out using a Horiba LabRAM HR Evolution system equipped with a 532 nm laser for excitation and a high spectral resolution grating of 1800 grooves/mm. The optical power P was tuned with a neutral-density filters, which reduces the laser power P from 100% down to 0.01%, and the laser spot size was determined to be ~2.6 μm for a 10× objective with a numerical aperture (NA) of 0.25.

Delta-mode measurements

The delta-mode technique was used for the bolomter measurements using a nanovoltmeter (Keithley 2182A) interfaced to a precision bipolar current source (Keithley 6220). The base T in our system was readout using the built-in silicon diode sensor (DT-670-CU-HT) underneath the Lakeshore sample stage (SH-2.00-T), as shown in Figure 3A. In the Kelvin sensing technique, the Keithley 6220 sources current in the range of 100 fA to 105 mA, and the nano voltmeter measures the ensuing voltage via the RS-232 communication channel with the trigger link cable 8501 for synchronization. The T is controlled using the Lakeshore 336 temperature controller interfaced to the DT-670-CU-HT, and a built-in heater warms the sample from the base T of ~3.88 K up to a maximum of 350 K. A Kelvin sensing technique was implemented to null-out the influence of the parasitic resistance R arising at the electrical contacts for the DUT and the external cabling of the instrumentation.

QUANTIFICATION AND STATISTICAL ANALYSIS

There are no quantification or statistical analyses to include in this study.

ADDITIONAL RESOURCES

Disclosures

Certain commercial equipment, instruments, software or materials, commercial or non-commercial, are identified in this paper in order to specify the experimental procedure adequately. Such identification is not intended to imply recommendation or endorsement by the National Institute of Standards and Technology, nor is it intended to imply that the materials or equipment identified are necessarily the best available for the purpose.